Parallel electric fields in the upward current region of the aurora: Indirect and direct observations

R. E. Ergun,[a] L. Andersson, D. S. Main, and Y.-J. Su
Laboratory for Atmospheric and Space Physics, University of Colorado, Boulder, Colorado 80303

C. W. Carlson, J. P. McFadden, and F. S. Mozer
Space Sciences Laboratory, University of California, Berkeley, California 94720

(Received 27 March 2002; accepted 20 May 2002)

In this article we present electric field, magnetic field, and charged particle observations from the upward current region of the aurora focusing on the structure of electric fields at the boundary between the auroral cavity and the ionosphere. Over 100 high-resolution measurements of the auroral cavity that were taken by the Fast Auroral Snapshot (FAST) satellite are included in this study. The observations support earlier models of the auroral zone that held that quasi-static parallel electric fields are the primary acceleration mechanism. In addition to the statistical study, several examples of direct observations of the parallel electric fields at the low-altitude boundary of the auroral cavity are put forth. These observations suggest that the parallel electric fields at the boundary between the auroral cavity and the ionosphere are self-consistently supported as oblique double layers. © *2002 American Institute of Physics.* [DOI: 10.1063/1.1499120]

I. INTRODUCTION

Our purpose in this article is to give a detailed statistical account of the electric fields in the upward current region of the aurora as observed by the Fast Auroral Snapshot (FAST) satellite and to present new observations of parallel electric fields and charged particle distributions at the ionospheric boundary of the auroral cavity. Many of the most conspicuous findings from the FAST satellite on the upward current region have been reported earlier[1–7] based on event analyses and small-sample surveys. We verify many of these findings with a large-sample study and, from that large-sample study, identify several instances of direct observations of the parallel electric field and examine the electric field signals and accompanying charged particle distributions in detail.

Parallel electric fields in the upward current region of the aurora were first inferred from studies of electron distributions[8] and in observations of ion beams.[9] The detection of converging electric field structures coined ''electrostatic shocks'' by the S3-3 satellite[10,11] and the Viking satellite[12] provided strong evidence of quasi-static, parallel electric fields in the upward current region of the aurora. The correlation of anti-earthward ion beams with electrostatic shocks[11,13] and the quantitative agreement between the ion beam energies and the inferred parallel potential of the converging electric field structures[14,15] established that parallel electric fields are the primary mechanism for the acceleration of charged particles in the auroral region.

Although it has been established that a parallel electric field can drive a current in a magnetic mirror geometry,[16] a theoretical understanding of how parallel electric fields are self-consistently supported in a collisionless plasma has not been established.[17] Theoretical treatments and models include weak double layers,[18] strong double layers,[19–22] anomalous resistivity,[23] and parallel electric fields associated with ion cyclotron waves.[24] Another approach based on the Alfvén–Fälthammar equations[25] suggests that more distributed electric fields are possible.

There also is no generally accepted model of how parallel electric fields are distributed along the flux tube between the plasma sheet and the ionosphere. S3-3 and subsequent satellite missions established that the auroral electron acceleration is a near Earth process, usually less than 8000 km in altitude, the S3-3 apogee.[13] Polar observations determined that the majority of auroral acceleration is below $2R_E$ in altitude.[26] The results of the Dynamics Explorer mission[27–29] and sounding rocket studies[30] suggested that there are two acceleration layers. FAST observations support the Dynamics Explorer studies and have identified a low altitude acceleration region.[6] Recent quasi-neutral modeling efforts corroborate the observationally-based model of two or more acceleration regions.[31]

Direct measurements of the parallel electric field in the upward current region[32] show amplitudes on the order of 100 mV/m suggesting strong double layers.[19] Observations in the downward current region[33–35] have conclusively determined that the parallel electric fields in that region are supported, at least in part, by strong double layers. We examine new electric field observations and the electron and ion distributions of the upward current region and suggest that the parallel electric field at the ionospheric boundary of the auroral cavity is self-consistently supported as an oblique double layer.

II. CURRENT OBSERVATIONAL UNDERSTANDING

We begin with a review of the prior modeling of the electric field structure of the aurora. Figure 1 depicts a two-dimensional, static model of the auroral potential structure that has emerged over years of research.[36] The auroral zone

[a]Also at the Department of Astrophysical and Planetary Sciences.

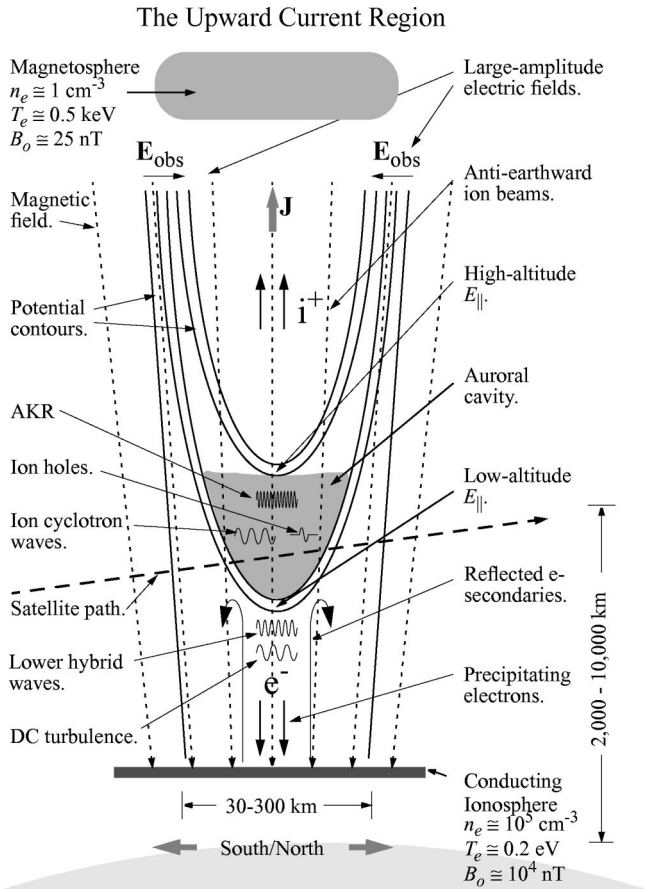

FIG. 1. A cartoon model of the upward current region of the aurora. The above model incorporates the concept of two regions of parallel electric fields.

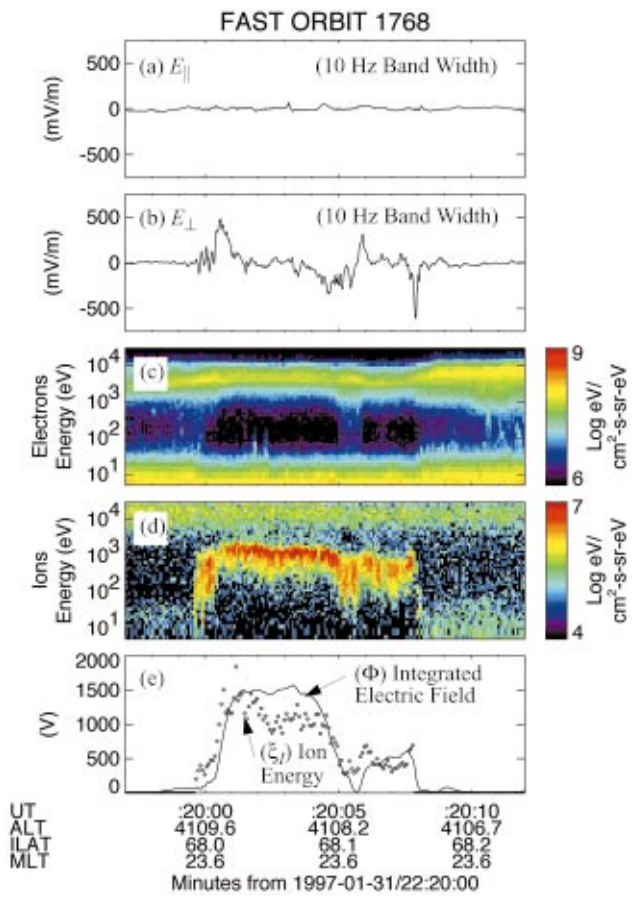

FIG. 2. (Color) High-time resolution observations of the auroral cavity in the upward current region. (a) $E_\parallel$ at a 10 Hz bandwidth. (b) $E_\perp$ at a 10 Hz bandwidth. (c) Electron energy flux, summed over all pitch angles, versus energy and time at 79 ms resolution. (d) Ion energy flux, summed over all pitch angles, versus energy and time. (e) The circles are the energy at which the ion fluxes peak (ξ_i). The solid line is Φ, the parallel potential inferred from the electric field observations [see Eq. (1)].

is bounded at high altitude by hot ($T_e \sim 0.5$ keV), tenuous ($n_e \sim 1$ cm^{-3}) magnetospheric plasma and at low altitude by cold ($T_e \sim 0.2$ keV), more dense ($n_e \sim 10^5$ cm^{-3}) ionospheric plasma that exhibits a finite conductivity. The near vertical dashed lines in Fig. 1 represent the Earth's magnetic field (**B**) which supports a mirror ratio between the magnetosphere and the ionosphere of roughly 400. The solid lines represent equipotential contours which embody a parallel electric field in the auroral acceleration region. The upward parallel electric field creates an anti-earthward ion beam and accelerates electrons earthward which, in turn, produce visible arcs.

Figure 1 reflects the concept that the parallel electric fields of the upward current region are confined to two or more layers[27,31] with the auroral cavity lying in between. The region below the low-altitude parallel electric field ($E_\parallel$) is dominated by ionospheric plasma. The ionospheric electron distribution includes precipitating electrons and their mirroring counterpart, auroral secondaries, and scattered primaries as well as a cold, dense population. The ionospheric ion distribution is a cold (~ 1 eV), gravitationally-bound combination of primarily O^+ and H^+ with He^+ as a minor constituent. The ion distributions are modified by perpendicular (to **B**) heating from plasma waves and low-frequency turbulence associated with the precipitating electrons. Inside the auroral cavity, the majority populations are electrons of magnetospheric origin and, often, ions of ionospheric origin. The ion beam in the auroral cavity is strongly modified by large-amplitude ion cyclotron waves, low-frequency turbulence, and ion phase-space holes. The auroral cavity also is the source region for auroral kilometric radiation (AKR). A notable finding is that there is little or no cold electron population within the auroral cavity.[4,5,7] Above the high-altitude parallel electric field, the magnetospheric plasma controls the electrodynamics.

Figure 2 displays plasma observations within the auroral acceleration region. The observations were made by the FAST Satellite. Similar presentations[1,2,6] have been made and instrument descriptions[37,38] have been reported, so our presentation is brief.

The horizontal axis in Fig. 2 represents 15 s of the near-midnight auroral zone at ~ 4000 km altitude. The satellite was moving from south to north through the auroral zone (see Fig. 1) during which it traversed approximately 80 km. The top panel, Fig. 2(a), displays the measured $E_\parallel$ filtered to a 10 Hz bandwidth. A wide band signal (~ 16 kHz, displayed later for other auroral crossings) typically has ion cyclotron waves with amplitudes on the order of 100 mV/m. The dc signal is, within error, zero along the flight path.

Figure 2(b) plots the dc electric field perpendicular to **B** in the direction closest to the spacecraft velocity (positive is mostly northward and nearly parallel to the satellite's velocity). The large positive excursion at ~22:20:01 UT is followed by a large negative deflection at ~22:20:08 UT. This signature is characteristic of a converging electric field structure as diagrammed in Fig. 1. Such electric field structures imply that an upward parallel electric field is located earthward of the spacecraft.

The electron energy flux is plotted in Fig. 2(c). The vertical axis represents energy and the color represents electron energy flux summed over all pitch angles. One can see a clear peak in energy flux at energies between 2 keV and 6 keV throughout the plot. The electron fluxes are relatively evenly distributed in pitch angle (not displayed) except for a loss-cone at 180° (anti-earthward). The net motion of the electrons is therefore earthward so these fluxes are identified as precipitating electrons that may create visible auroral arcs.

Panel 2(d) displays the ion energy flux in the same format. An ion beam stands out at roughly 1–2 keV traveling anti-earthward. From ~22:20:01 UT until ~22:20:08 UT, there are downward (earthward) accelerated electrons and an up-going (anti-earthward) ion beam. The energy of the peak electron fluxes decreases but remains at several kilovolts when the ion beam is present, so we conclude that there is a parallel electric field both above and below the spacecraft. Figure 1 suggests a possible path of the spacecraft though the auroral model that would yield a similar, albeit less-complex rendering of the observations in Fig. 2.

The bottom panel, Fig. 2(e), plots the ion beam energy (ξ_I circles) and the inferred parallel potential (Φ). The ion beam energy ($\xi_I = e\Psi/J$) is derived from the ratio of the energy flux (Ψ) to the current density (J) for each of the measured ion distributions in Fig. 1(d). Plasma sheet ions (highest energy) are excluded in determining ξ_I. The inferred parallel potential is derived by integrating the observed electric field from the left edge of the plot (t_0 = 22:19:57 UT) where Φ is assumed to be zero:

$$\Phi(t) = \int_{t_o}^{t} (\mathbf{E}(t') - \mathbf{E}_I) \cdot \boldsymbol{\nu}_{sc} dt', \tag{1}$$

where $\boldsymbol{\nu}_{sc}$ is the spacecraft velocity. $\mathbf{E}_I$, 10 mV/m in this example, is an estimate of a constant ionospheric electric field projected to the altitude of the spacecraft that is required to best fit Φ to the ion beam energy. The implied parallel potential and the ion beam energy are within ~50% when the ion beam energy was greater than 100 eV. The agreement between the two quantities implies that the ion beam is energized by a parallel electric field that is static for more than 8 s, providing strong, indirect evidence of quasi-static, parallel electric fields.

III. STATISTICAL STUDIES: INDIRECT OBSERVATIONS

One-hundred high-resolution snapshots of the auroral region were examined with the same techniques that were used in the above example. One of main objectives of the study, besides searching for direct observations of parallel electric fields, was to determine a statistical relationship between the ion beam energy (ξ_I) and the implied parallel potential (Φ) that is determined from the measured electric field. For each of the orbits a procedure was executed to determine ξ_I at 79 ms intervals (the standard "burst" resolution of the FAST particle detectors) and the corresponding value of Φ. The selected events were all in the near-midnight region, endured between 2 s and 20 s, and had verifiable electric fields (e.g., the instrument was in the proper biasing state, not saturated, and was not acquiring data during a terminator crossing). The events were selected by inspecting 5 s resolution ion spectrograms for evidence of anti-earthward ion beams, thus, for example, strong field-aligned electron precipitation events during substorm expansions were often not included because of no clear ion beam signature. The results are also restricted to altitudes of less than 4,175 km, the apogee of the FAST satellite, and to periods when the FAST satellite was in "burst" mode,[38] so high-resolution data are available.

$\mathbf{E}_I$ is constant and is determined by two methods. Method 1, the "least-squares" method, determines $\mathbf{E}_I$ with a least-squares fit between Φ and ξ_I. Method 2, the "forced-zero" method, determines $\mathbf{E}_I$ by forcing $\Phi = 0$ at both edges of the ion beam. Method 2 requires that high-resolution data are available for both edges of the ion beam, so the two studies did not use the same set of auroral crossings. In no case did $\mathbf{E}_I$ exceed 60 mV/m.

Figure 3 plots a summary of the results of 100 auroral cavity events which includes more than 10,000 ion distributions. In Figs. 3(a) and 3(b), the horizontal axis represents ξ_I and the vertical axis represents Φ. Only samples with $\xi_I > 100$ eV and peak energy fluxes greater than 10^6 cm^{-2} s^{-1} sr^{-1} were considered. Figure 3(a) shows a linear agreement of the two quantities over two orders of magnitude with a standard deviation of 28%. The example in Fig. 2 has a standard deviation of 36%, so it is slightly worse than a "typical" example. Other examples can be found in Figs. 4–6. The linear agreement is somewhat forced by the selection of the free parameter $\mathbf{E}_I$. It is of importance, then, that $\mathbf{E}_I$ is always within observed values of the ionospheric electric fields.

Figure 3(c) is a histogram of the standard deviation of each of the 100 auroral cavity events:

$$\mathrm{Err}_n = \frac{(\xi_{In} - e\Phi_n)}{\xi_{In}}.$$

The histogram in Fig. 3(c) has a nearly Gaussian shape, indicating that the differences between the integrated electric field and the ion beam energy are somewhat random. There are several possible sources that could contribute to these differences. The values of ξ_I have a larger scatter about the mean or "noise" than does Φ [e.g., Fig. 2(e) from 22:20:00 UT to 22:20:01 UT]. This noise in ξ_I produces part of the 28% standard deviation. The "noise" in ξ_I is partly statistical (e.g., the square root of total counts) but may be also due to strong wave–particle interactions which is discussed later in this article. There are also offsets between ξ_I and Φ that endure for several seconds. For example, between 22:20:02 UT and 22:20:04 UT in Fig. 2(b), Φ averages ~1500 V

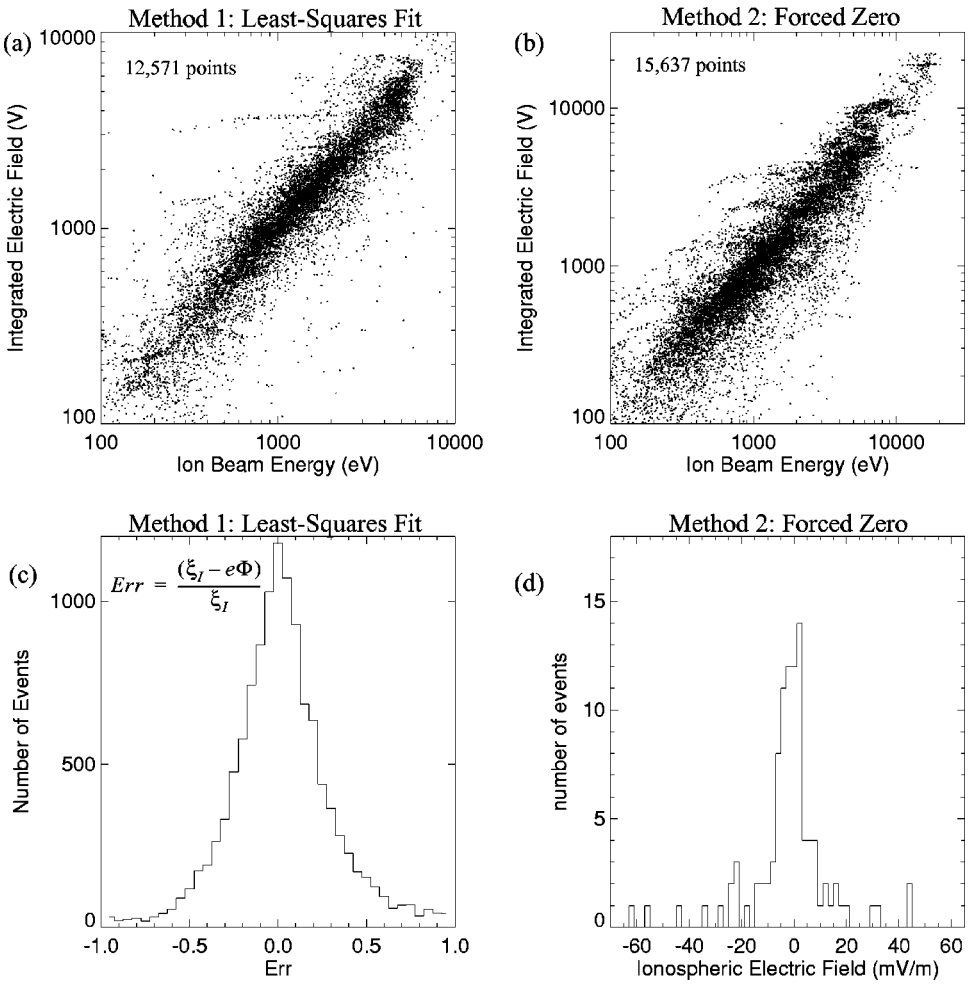

FIG. 3. The results of a statistical study comparing energy at which the ion fluxes peak (ξ_I) to the inferred potential from the electric field measurement [Φ, see Eq. (1)]. (a) A scatter plot of 12,571 individual ion distributions in which the ionospheric electric field was determined by a least-squares fit between ξ_I and Φ. (b) A scatter plot of 15,637 individual ion distributions in which the ionospheric electric field was determined by forcing $\Phi = 0$ at the edge of the ion beam. (c) A histogram of the standard deviation from a linear fit. The near-Gaussian distribution indicates random errors of ~28%. (d) A histogram of the ionospheric electric fields.

whereas ξ_I averages ~1100 eV. The longer-term offset in this example could be caused by a localized ionospheric electric field of ~50 mV/m or by a temporal change in the electric field structure.

Figure 3(b) shows the same linear agreement as in Fig. 3(a) and a nearly similar standard deviation (~30%). In Method 2, $\mathbf{E}_I$ is determined only from the end points of the ion beam and the linear agreement is not "forced" as in the least-squares method. A histogram of $\mathbf{E}_I$ is plotted in Fig. 3(d). The histogram shows a somewhat random distribution with none of the absolute values exceeding 60 mV/m.

Figure 3 demonstrates via two methods a linear agreement between the ion beam energy (ξ_I) and the integrated electric field (Φ) with a roughly 30% standard deviation. The auroral model predicts that Φ and ξ_I are equal if the electric field is static and the ionospheric electric field is zero. We conclude that the FAST observations lend compelling support to the auroral model of quasi-static parallel electric fields. This larger study supports the earlier reports on FAST satellite observations that were based on small-survey results and single-event analysis.[1,2,6]

IV. DIRECT OBSERVATIONS OF THE PARALLEL ELECTRIC FIELD AT THE IONOSPHERIC BOUNDARY OF THE AURORAL CAVITY

The statistical study, while providing conclusive indirect evidence that parallel electric fields are the primary acceleration mechanism, do not yet explain the distribution of the parallel electric fields along the magnetic flux tube nor how they are self-consistently supported. Here, we put forth several examples of direct observations of parallel electric fields and the accompanying charged particle observations that suggest a localized structure at the ionospheric boundary of the auroral cavity.

A. Direct observations of $E_\parallel$

Figures 4–6 display five auroral cavity observations chosen from the 100-event study. Figures 4 and 5 have the same format used in Fig. 2. Figure 6 has two additional panels which are discussed later. The events were selected because they all display parallel electric fields greater than 100 mV/m that can be validated.

Validation of the parallel electric fields involves several steps. The instrument is confirmed to be satisfactorily operating in the proper biasing state. None of the individual probes can be saturated and the spacecraft cannot be changing modes, magnetically torquing, or crossing the terminator. The parallel electric field is derived with two different techniques in the cases where the data are available (orbits 1800 and higher). One technique uses the individual signals from four probes that form a tetrahedron.[38] Three of the probes are ~28 m from the spacecraft and in the spacecraft spin plane. The fourth probe is ~4 m from the spacecraft along the spin axis. $E_\parallel$ is calculated from the dot product of the vector

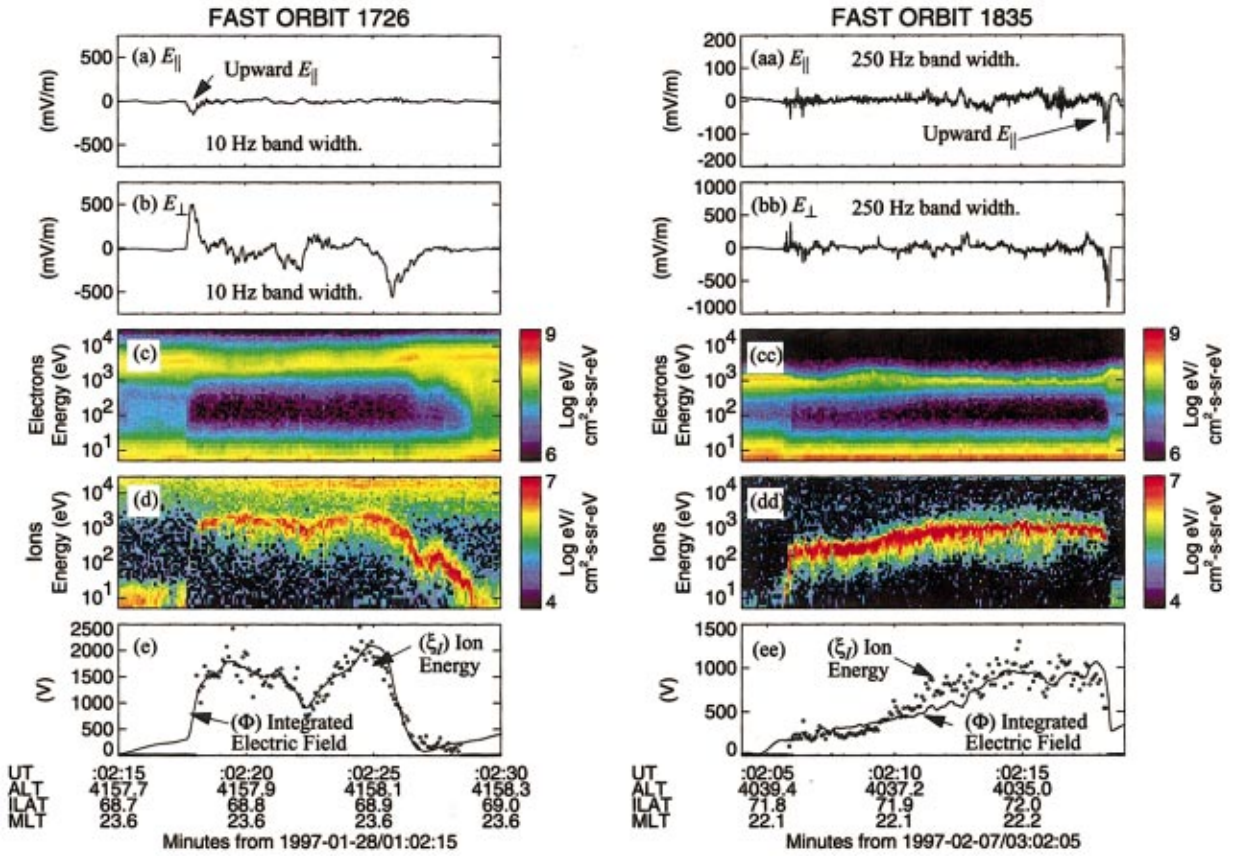

FIG. 4. (Color) Two examples of the parallel electric field at the ionospheric boundary of the auroral cavity. The display is similar to that in Fig. 2. (a, aa) $E_\parallel$. (b, bb) $E_\perp$. (c, cc) Electron energy flux versus energy and time at 79 ms resolution. (d, dd) Ion energy flux versus energy and time. (e, ee) A comparison of the energy at which the ion fluxes peak (ξ_I) and Φ, the integrated electric field along the spacecraft path.

electric field derived in the rotating frame of the spacecraft from the four probes and the measured magnetic field in the rotating frame of the spacecraft. The spin tone and second harmonic is then removed from the signal. We label this signal from the mathematical derivation, $\mathbf{E}\cdot\mathbf{B}/|\mathbf{B}|$.

The second technique uses only the spin-plane probes (all 28 m from the spacecraft), and assumes the electric field along the spin axis is zero. Since the magnetic field is within 6° of the spin plane of the spacecraft, the contribution of the short, 4 m axis should be small. We call this signal **E** *near* **B**. Comparing the two signals derived by the two different techniques is essentially a test that the short (4 m) axis does not dominate the parallel electric field signal and that a signal detected in **E** *near* **B** is not from an extremely large field along the spacecraft axis. The parallel electric field is validated if both signals exceeded 100 mV/m and do not differ by more than 50 mV/m. Finally, the root-mean-square value of the parallel electric field signal (at a 10 Hz bandwidth) over a 30 s–60 s period surrounding the event must be less than 25 mV/m.

Of the 100 auroral cavity crossings that were examined, the parallel electric fields in 84 crossings were, within error, zero (error levels were between ± 20 mV/m and ± 50 mV/m, depending on the plasma parameters). Five of the auroral crossings (all displayed) have validated parallel electric fields greater than 100 mV/m. One crossing, Fig. 6, has two parallel electric field events. The remaining 11 events did not have a valid parallel electric field greater than 100 mV/m nor could we verify that the signal was, within error, zero. We caution the reader not to draw strong statistical conclusions since the number of validated events depends on the validation process. Furthermore, naturally occurring parallel electric fields that have amplitudes less than the accuracy of the measurement ($<20-50$ mV/m) would be considered to be zero, so such fields are not included in this study.

The parallel electric field signals in Figs. 4 and 6 show a brief negative excursion (negative is upward in the northern hemisphere) at the boundary of the auroral cavity. The >100 mV/m parallel electric fields appear in regions of strong field-aligned currents at the edge of the ion beam that abruptly emerges (or abruptly vanishes), and occur in conjunction with a significant $E_\perp$. The amplitude of $E_\parallel$ has been observed to be as high as 300 mV/m. An accurate relative velocity between the structure and the spacecraft has not been established in any of the examples so the net potential of the parallel electric field is unknown. These observations are similar in amplitude, duration, and position (at the edge of the ion beam) as those reported from Polar.[32] Observations in Figs. 4–6 are from the northern hemisphere whereas the published Polar observations[32] are from the southern hemisphere; hence the difference in sign. The large amplitude and the short duration of $E_\parallel$ suggest oblique double layers may be present at the ionospheric boundary of the auroral cavity.[19–22]

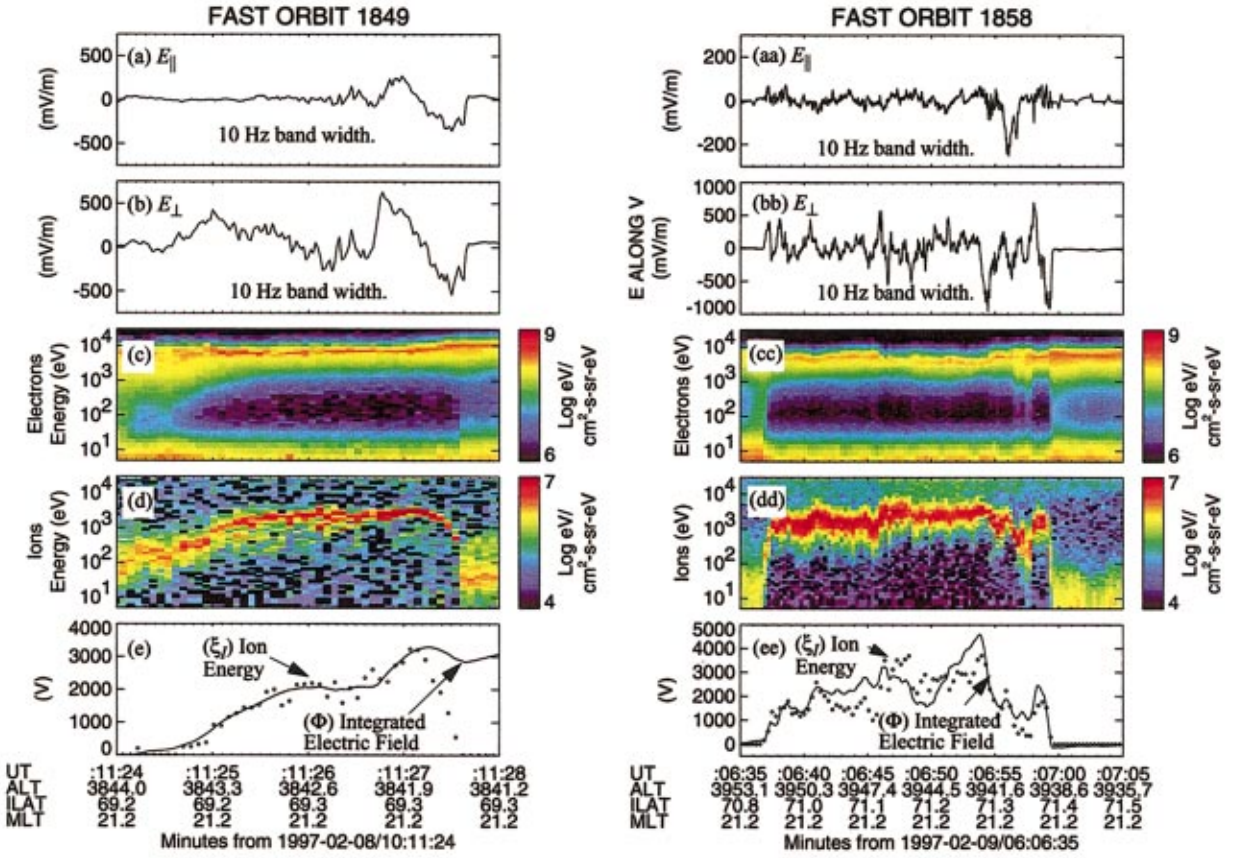

FIG. 5. (Color) Two examples of the parallel electric fields in the auroral cavity. (a, aa) $E_\parallel$. (b, bb) $E_\perp$. (c, cc) Electron energy flux versus energy and time at 79 ms resolution. (d, dd) Ion energy flux versus energy and time. (e, ee) A comparison of the energy at which the ion fluxes peak (ξ_I) and Φ, the integrated electric field along the spacecraft path.

An interesting feature, also visible in the examples published from Polar observations,[32] is the asymmetry in $E_\parallel$. $E_\parallel$ rises abruptly to its maximum value on the ionospheric side and displays a less abrupt decay back to zero once the ion beam appears. The signals display a higher level of turbulence on the auroral cavity side. This asymmetry may give an excellent clue to the self-consistent nature of $E_\parallel$ which we discuss in a separate article.[39]

The two examples in Fig. 5 somewhat differ from those in Figs. 4 and 6 and those observed by Polar.[32] The parallel electric field in the orbit 1849 crossing, Fig. 5(a) (some of these data were previously published[1]) indicates a wave-like structure abruptly ending at the ionospheric boundary of the auroral cavity (10:11:26.0 UT to 10:11:27.5 UT). There is no detectable (~2 nT resolution) magnetic signature, so we surmise that an electrostatic structure such as an ion phase-space hole[40] is growing at the cavity boundary or traveling along the cavity boundary. Interestingly, the integrated electric field and the peak energy of the ion beam [Fig. 5(e)] agree from the left side of the plot until the wave event is seen at ~10:11:27 UT, after which they diverge. The wave-like electrostatic structure may have significantly altered the large-scale potential structure during this event.

The parallel electric field during orbit 1858, Fig. 5(aa), at first glace, appears inside of the auroral cavity rather than at the ionospheric boundary. A close examination, however, reveals that the peak energy of the ion fluxes decreases abruptly and falls nearly to zero at the right edge of the parallel electric field as seen in Figs. 5(dd) and 5(ee) at ~06:06:57 UT. One could interpret the period between 06:06:57 UT and 06:07:00 UT as a separate auroral cavity. Thus, the example in orbit 1858 does not differ dramatically from the events in Figs. 4 and 6 or the Polar observations that are at the edge of the auroral cavity.

B. Plasma waves

The plasma waves at the ionospheric boundary of the auroral cavity can be important in determining the self-consistent nature of $E_\parallel$. Figure 6(e) displays the wave electric field spectral power density as a function of frequency (40 Hz–16 kHz at 40 Hz resolution) and time (0.5 s resolution). A clear change in the nature of the plasma waves is seen at the boundaries of the auroral cavity at 04:59:53 UT and at 05:00:10 UT. Inside the auroral cavity, strong turbulence is primarily below the H^+ cyclotron frequency, the white line in Fig. 6(e), whereas quasi-electrostatic whistler waves with frequencies just above the lower hybrid frequency dominate the power outside of the cavity.

Figure 7 plots an expanded view (5 s) of the ionospheric boundary on the right-hand side of Fig. 6 where the FAST satellite was in "burst" mode acquiring high-time resolution data. The top two panels, Figures 7(a) and 7(b), display $E_\parallel$ and $E_\perp$ at ~16 kHz bandwidth in black and at ~10 Hz

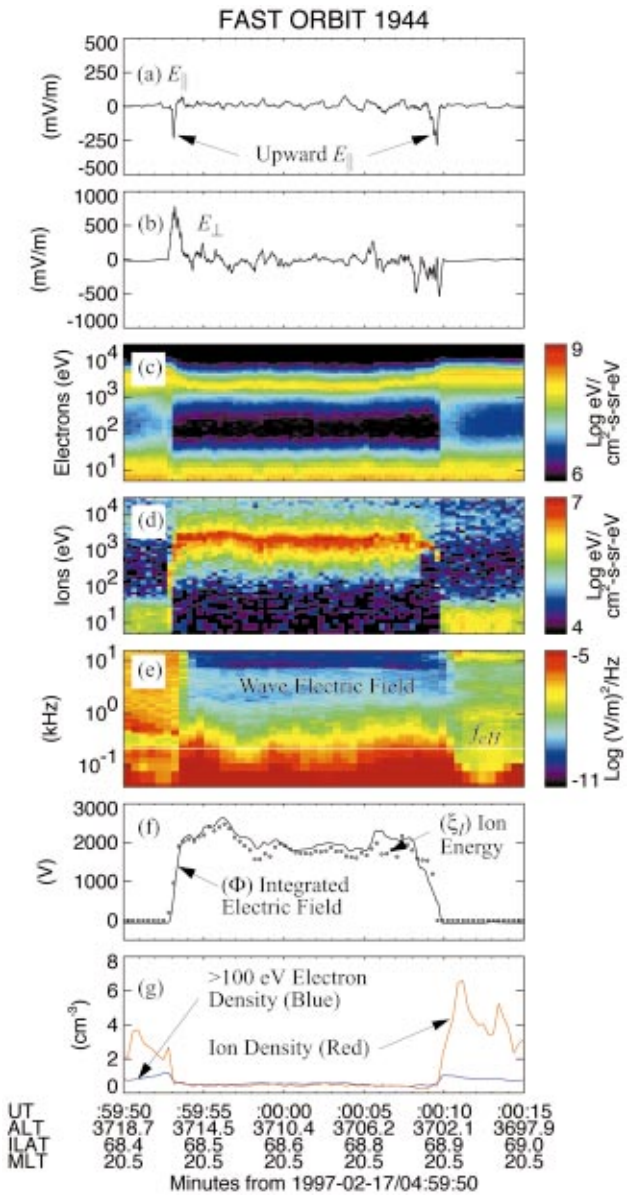

FIG. 6. (Color) Parallel electric fields at the ionospheric boundary on both sides of the auroral cavity. (a) $E_\parallel$ at a 10 Hz bandwidth. (b) $E_\perp$ at a 10 Hz bandwidth. (c) Electron energy flux versus energy and time at 316 ms resolution. (d) Ion energy flux versus energy and time at 316 ms resolution. (e) The omni-directional wave spectral power density as a function of frequency and time. The y-axis spans 40 Hz to 16 kHz in frequency at 40 Hz resolution. Each spectra averages over 0.5 s. The white line is the H^+ cyclotron frequency. (f) A comparison of the energy at which the ion fluxes peak (ξ_I) and the integrated electric field along the spacecraft path. (g) The plasma density as determined from the ~5 eV to 30 keV ion distribution (red trace) and the energetic (>100 eV) electron distribution (blue trace).

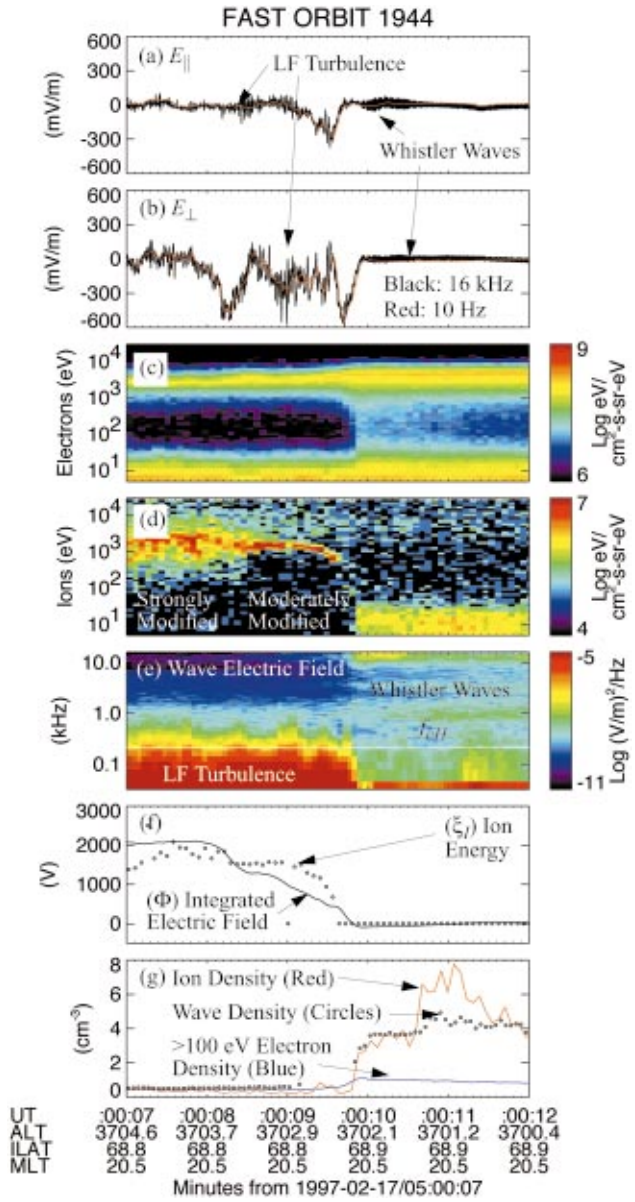

FIG. 7. (Color) An expanded view of the right-hand boundary of the auroral cavity from Fig. 6. (a) $E_\parallel$ at a 10 Hz bandwidth (red) and at a 16 kHz bandwidth (black). (b) $E_\perp$ at a 10 Hz bandwidth (red) and at a 16 kHz bandwidth (black). (c) Electron energy flux versus energy and time at 79 ms resolution. (d) Ion energy flux versus energy and time at 79 ms resolution. (e) The omni-directional wave spectral power density as a function of frequency and time. The y-axis spans 40 Hz to 16 kHz in frequency at 40 Hz resolution. Each spectra averages over 128 ms. (f) A comparison of the energy at which the ion fluxes peak (ξ_I) and the integrated electric field along the spacecraft path. (g) The plasma density as determined from the ion distribution (red trace), the energetic electron distribution (blue trace), and from characteristics of the wave emissions (circles).

bandwidth in red. An omni-directional spectra (the combined spectra of $E_\parallel$ and $E_\perp$) is displayed in Fig. 7(e). The two wide-band traces and the wave spectra illustrate the difference in the nature of the plasma waves between the auroral cavity and the ionosphere. The intense turbulence inside of the auroral cavity on the left side of Figs. 7(a), 7(b), and 7(e) has characteristic frequencies less than ~200 Hz, the H+ cyclotron frequency. The characteristic frequencies rise to >1 kHz outside the cavity (right-hand side). Within the auroral cavity, ion phase-space holes are often seen embedded in the low-frequency turbulence. Figure 8 displays the bipolar $E_\parallel$ signature of a pair of ion phase-space holes[6,40] seen inside of the auroral cavity of the orbit 1944 event.

C. Plasma density

A significant change in plasma density is seen at the ionospheric boundary in Figs. 6 and 7. Figure 6(g) plots the plasma density derived from two different techniques. The red trace represents the plasma density derived from the ion

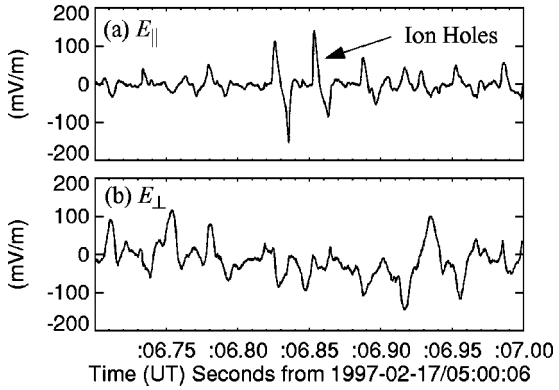

FIG. 8. A magnified view (0.3 s) of the electric fields inside of the auroral cavity from Fig. 6. (a) $E_{\|}$ at a 16 kHz bandwidth. (b) $E_{\perp}$ at a 16 kHz bandwidth. The bipolar structures in $E_{\|}$ are characteristic of ion phase-space holes.

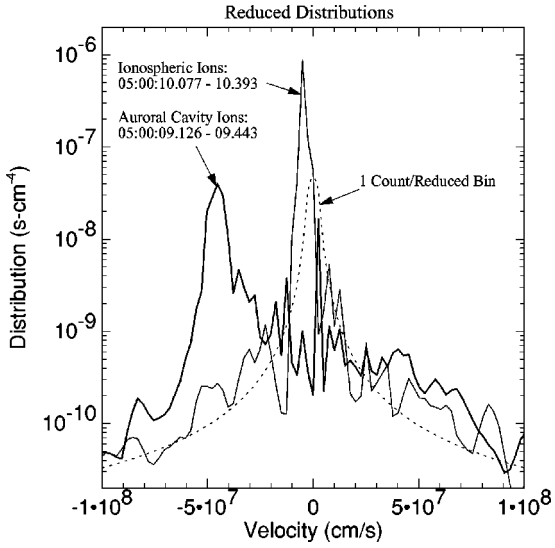

FIG. 9. Reduced one-dimensional (1-D) ion distributions within the auroral cavity (thick line) and in the ionosphere (thin line). The ions are assumed to be H^+. The dashed line is the 1-count level in a reduced bin. Both of the distributions are near the boundary between the auroral cavity and the ionosphere. Since the satellite travels mostly perpendicular to B, the distributions are from adjacent flux tubes.

distribution which measured from ~5 eV to 25 keV fluxes. The derived densities assumed a H^+ plasma. The blue trace is the plasma density derived from the energetic part (>100 eV) of the electron distribution. At energies less than ~100 eV, spacecraft photoelectrons dominate the measured electron distribution so these data are discarded. The plasma densities derived from the two different techniques agree within the auroral cavity indicating an average density of ~0.4 cm^{-3}. At the boundaries of the cavity, a steep gradient results in an increase in plasma density as measured by the ion distribution. Outside the cavity, the density derived from the "hot" (>100 eV) electron distributions do not agree with the ion density indicating a substantial "cold" (<100 eV) electron population.

Figure 7(g) plots the densities derived from the ion and electron distributions at higher time resolution than in Fig. 6(g) and includes the plasma density (circles) estimated from the plasma cutoff or a fit of the ratio $E_{\|}^2(\omega)/E_{\perp}^2(\omega)$ to the whistler dispersion.[4,5] The values are plotted only if a clear plasma cutoff or a good fit to the whistler dispersion is found. This estimate of plasma density is accurate to within a factor of 2. One can see that both the ion density and the density derived from the wave dispersion indicate a significant increase in plasma density, about a factor of 10, between the auroral cavity and the ionosphere. The two densities differ by a factor of 2 for a short period outside the cavity (~05:00:10.7 UT–~05:00:11.4 UT) which may be due to an O^+ population or to L-mode or electron acoustic waves corrupting the wave-dispersion fits. Inspection of the 100 auroral cavity events indicates that such density gradients are characteristic of the ionospheric boundary of the auroral cavity.

D. Electron and ion distributions

The electron and ion distributions at the ionospheric boundary of the auroral cavity reveal valuable clues on the acceleration process. Unfortunately, there are several confounding issues. Intense plasma waves on both sides of the boundary, for example those displayed in Figs. 7(a), 7(b), and 7(e), can rapidly alter the distributions and make analysis more difficult. Another issue is that the spacecraft travels nearly perpendicular to **B** in the auroral zone, so one cannot measure distributions functions on both sides of a parallel electric field on the same magnetic flux tube.

The ion and electron distributions indicate that the net potential between the magnetosphere and the ionosphere in the event in Fig. 7 is roughly constant at ~5 kV. Within the cavity, the electron energy fluxes in Fig. 7(c) peak at ~3.4 kV whereas the ion energy fluxes in Figs. 7(d) and 7(f) peak at ~1.6 kV. On the ionospheric side, the electron energy fluxes peak at ~5 kV. Thus, the simple diagram in Fig. 1 is representative in this case.

Ion distributions within the cavity differ dramatically from those in the ionosphere. Figure 9 displays distribution functions inside the auroral cavity and in the ionosphere immediately adjacent to the auroral cavity. In both distributions, the ions were assumed to be H^+. The ionospheric distribution (thin solid line) shows moderately dense (~4 cm^{-3}), cold ($T_{i\|}$~3 eV) population drifting anti-earthward (or toward the auroral cavity) at ~50 km/s. The auroral cavity distribution has a considerably lower density (~0.4 cm^{-3}), higher temperature ($T_{i\|}$~900 eV; the isolated ion beam, plasma sheet ions excluded, has a parallel temperature of roughly 350 eV) and a significantly faster drift (~460 km/s). In Fig. 7(d), one can see that the ion distributions inside the auroral cavity change character. Near the ionospheric boundary (~05:00:08.5 UT to ~05:00:09.8 UT) the ion beam is relatively mono-energetic yet already shows a moderate parallel heating. The ion beams from ~05:00:07.0 UT to ~05:00:08.5 UT, however, display strong parallel heating.

The auroral cavity distribution and the ionospheric distribution clearly cannot be related by a simple adiabatic mapping through a parallel electric field (the magnetic mirror force does not significantly contribute over such a short dis-

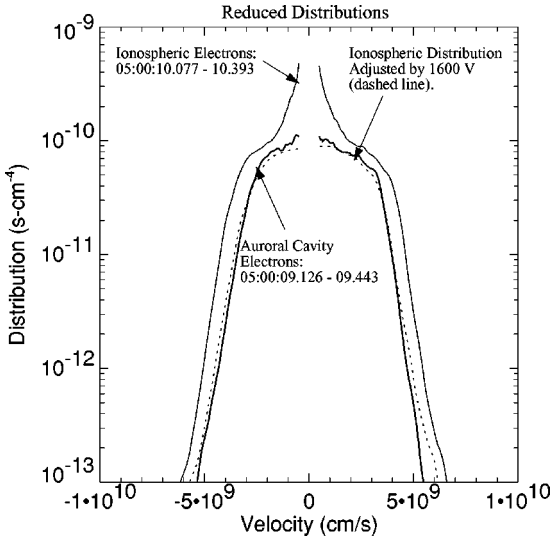

FIG. 10. Reduced 1-D electron distributions within the auroral cavity (thick line) and in the ionosphere (thin line). The dashed line is the ionospheric distribution adjusted by 1600 V representing an adiabatic evolution through a parallel electric field. Both of the distributions are near the boundary between the auroral cavity and the ionosphere. Since the satellite travels mostly perpendicular to **B**, the distributions are from adjacent flux tubes.

tance). The distributions that travel from the ionosphere into the auroral cavity have been considerably modified. Strong, low-frequency turbulence is seen throughout the auroral cavity in almost all the 100 cases that were studied. Wave amplitudes are most often >100 mV/m and reach more than 1 V/m. It is very likely, then, that wave–particle interactions alter the ion beam emerging from the parallel electric field into a heated, drifting population.

Ironically, the ionospheric and auroral cavity electron distributions can be better related by a simple adiabatic mapping through a parallel electric field. Figure 10 displays electron distributions inside of the auroral cavity (thick line) and in the ionosphere (thin line), both near the boundary between the ionosphere and the auroral cavity. The distribution below ~ 100 V has been removed because of possible contamination by spacecraft photoelectrons so the ionospheric distribution may have a cold core that is not displayed. The dotted line in Fig. 10 is the ionospheric distribution adjusted by 1600 V representing an adiabatic evolution through a parallel electric field. It is assumed that the evolved distribution would not be greatly affected by the mirroring magnetic field due to the short distances (on the order of 10 km). The adjusted ionospheric distribution and the distribution from inside of the cavity correspond well even though the two distributions were not taken on the same magnetic flux tube.

V. DISCUSSION AND CONCLUSIONS

A 100-event study supports many of the published features of the auroral cavity that were based on single-event analyses and small-sample surveys from the FAST satellite,[1,2,6] event analyses from the Viking satellite,[12] and large-sample surveys from the S3-3 satellite.[11,15] The quiescent auroral cavity can be well described by a static potential structure that carries a parallel electric field with the caveat that the observations display a considerably more complex structure. The potential derived from the integrated electric field and that derived from the ion beam energy quantitatively agree providing, in total, compelling indirect evidence of parallel electric fields. FAST observations and Dynamics Explorer observations[27–29] support a model[31] that includes both a high- and low-altitude parallel electric field.

Direct observations of the parallel electric fields in the upward current region from the Polar satellite[32] and the examples presented here from the FAST satellite indicate that the parallel electric field at the ionospheric boundary of the auroral cavity may be localized to a thin layer. An amplitude of ~ 100 mV/m indicates that the parallel electric field extends on the order of 10 km along the magnetic flux tube, roughly 10 Debye lengths (λ_D) in the auroral cavity and approximately $100\lambda_D$ using ionospheric parameters. The observed parallel electric fields are at the ionospheric boundary of the auroral cavity with a substantial $E_\perp$. Often $E_\perp > E_\parallel$ and the ion beam is seen to abruptly appear or vanish.

The ionospheric boundary of the auroral cavity is characterized by an order-of-magnitude change in the plasma density over a short distance from the cavity to the ionosphere. The density gradient in Fig. 7(g) occurs in ~ 100 ms during which the satellite traveled 500 m. This scale is on the order of $\sim 1-5\lambda_D$ and ~ 5 ion gyroradii [the perpendicular ion temperature $O(100)$ eV in the cavity] indicating a thin boundary.

Intense turbulence with frequencies below the H^+ cyclotron frequency and ion phase-space holes are almost always observed within the auroral cavity. The amplitude of the turbulence inside of the auroral cavity is on the order of 100 mV/m which suggests that strong modification of the charged particle distributions is possible. Intense whistler and lower hybrid emissions are seen on the ionospheric side of the cavity boundary. The electron fluxes traveling earthward may be unstable as they emerge from the parallel electric field at the ionospheric boundary of the auroral cavity.

The ionospheric ion distributions indicate a relatively cold population (~ 3 eV) drifting anti-earthward and therefore toward the parallel electric field. Interestingly, the observed drift velocity in the spacecraft frame is adequate to satisfy the Bohm criterion for a stationary double layer. The accelerated ion distribution inside of the auroral cavity indicates rapid parallel heating, an observation that is consistent with the intense low-frequency turbulence that is characteristic of the auroral cavity. The anti-earthward traveling ion beam often contributes the majority of the plasma density in the auroral cavity and the hot plasma sheet ions make up the remainder.

A comparison of the electron distributions on either side of the ionospheric boundary of the auroral cavity indicates that the distributions adiabatically evolve through the parallel electric field. The majority of the cold ionospheric electron fluxes are reflected by the parallel electric field at the boundary of the auroral cavity. A portion of the precipitating electrons fluxes that are reflected or scattered in the ionosphere and the secondary electron fluxes that they emit have sufficient energy to penetrate the parallel electric field and constitute a little less than one half of the auroral cavity electron

density. This electron population may play a large role in the location and structure of the parallel electric fields. The accelerated electron fluxes emerging into the ionosphere may be unstable which is consistent with the intense lower hybrid and electrostatic whistler waves.

Direct observations of parallel electric fields have now been verified by two different satellite instruments, albeit with a similar design. Although the statistics are uncertain, parallel electric fields with amplitudes >100 mV/m are detected in roughly 5% of the low-altitude (<4175 km) auroral cavity crossings determined by the presence of an ion beam in the FAST satellite survey. No similar statistic is available from the Polar satellite survey, however, the detection rate of the parallel electric field of these amplitudes is very roughly what would be expected. The observed electric field structures, ion distributions, and electron distributions suggest that the ionospheric boundary of the auroral cavity appears to be self-constantly supported by an oblique, asymmetric double layer.

ACKNOWLEDGMENTS

This work is supported by NASA Grants No. NAG5-120026, No. NAG5-3596, and NSF Grant No. ATM-0202564.

[1]J. P. McFadden, C. W. Carlson, R. E. Ergun, F. S. Mozer, M. Temerin, W. Peria, D. M. Klumpar, E. G. Shelley, W. K. Peterson, E. Moebius, L. Kistler, R. Elphic, R. Strangeway, C. Cattell, and R. Pfaff, Geophys. Res. Lett. **25**, 2021 (1998).
[2]R. E. Ergun, C. W. Carlson, J. P. McFadden, F. S. Mozer, G. T. Delory, W. Peria, C. C. Chaston, M. Temerin, R. Elphic, R. Strangeway, R. Pfaff, C. A. Cattell, D. Klumpar, E. Shelley, W. Peterson, E. Moebius, and L. Kistler, Geophys. Res. Lett. **25**, 2025 (1998).
[3]E. Möbius, L. Tang, L. M. Kistler, M. Popecki, E. J. Lund, D. Klumpar, W. Peterson, E. G. Shelley, B. Klecker, D. Hovestadt, C. W. Carlson, R. Ergun, J. P. McFadden, F. Mozer, M. Temerin, C. Cattell, R. Elphic, R. Strangeway, and R. Pfaff, Geophys. Res. Lett. **25**, 2029 (1998).
[4]R. J. Strangeway, L. Kepko, R. C. Elphic, C. W. Carlson, R. E. Ergun, J. P. McFadden, W. J. Peria, G. T. Delory, C. C. Chaston, M. Temerin, C. A. Cattell, E. Moebius, L. M. Kistler, D. M. Klumpar, W. K. Peterson, E. G. Shelley, and R. F. Pfaff, Geophys. Res. Lett. **25**, 2065 (1998).
[5]R. E. Ergun, C. W. Carlson, J. P. McFadden, F. S. Mozer, G. T. Delory, W. Peria, C. C. Chaston, M. Temerin, R. Elphic, R. Strangeway, R. Pfaff, C. A. Cattell, D. Klumpar, E. Shelley, W. Peterson, E. Moebius, and L. Kistler, Geophys. Res. Lett. **25**, 2061 (1998).
[6]J. P. McFadden, C. W. Carlson, and R. E. Ergun, J. Geophys. Res. **104**, 14453 (1999).
[7]J. P. McFadden, C. W. Carlson, R. E. Ergun, D. M. Klumpar, and E. Moebius, J. Geophys. Res. **104**, 14671 (1999).
[8]D. S. Evans, J. Geophys. Res. **79**, 2853 (1974).
[9]E. G. Shelley, R. D. Sharp, and R. G. Johnson, Geophys. Res. Lett. **3**, 654 (1976).
[10]F. S. Mozer, C. W. Carlson, M. K. Hudson, R. B. Torbert, B. Parady, J. Yatteau, and M. C. Kelley, Phys. Rev. Lett. **38**, 292 (1977).
[11]E. L. Bennett, M. Temerin, F. S. Mozer, and M. H. Boehm, Geophys. Res. Lett. **88**, 7107 (1983).
[12]L. P. Block, C.-G. Falthammar, P.-A. Lindqvist, G. Marklund, and F. S. Mozer, Geophys. Res. Lett. **14**, 435 (1987).
[13]F. S. Mozer, C. A. Cattell, M. K. Hudson, R. L. Lysak, M. Temerin, and R. B. Torbert, Space Sci. Rev. **27**, 155 (1980).
[14]M. Temerin, M. H. Boehm, and F. Mozer, Geophys. Res. Lett. **8**, 799 (1981).
[15]M. S. Redsun, M. Temerin, F. S. Mozer, and M. H. Boehm, J. Geophys. Res. **90**, 9615 (1985).
[16]S. Knight, Planet. Space Sci. **21**, 741 (1973).
[17]J. E. Borovsky, J. Geophys. Res. **98**, 6101 (1993).
[18]M. Temerin, K. Cerny, W. Lotko, and F. S. Mozer, Phys. Rev. Lett. **48**, 1175 (1982).
[19]L. P. Block, Cosm. Electrodyn. **3**, 349 (1972).
[20]J. R. Kan, J. Geophys. Res. **80**, 2089 (1975).
[21]D. W. Swift and J. R. Kan, J. Geophys. Res. **80**, 985 (1975).
[22]D. W. Swift, J. Geophys. Res. **84**, 6427 (1979).
[23]M. K. Hudson and F. S. Mozer, Geophys. Res. Lett. **5**, 131 (1978).
[24]S. Ishiguro, T. Sato, H. Takamaru, and The Complexity Simulation Group, Phys. Rev. Lett. **78**, 4761 (1997).
[25]J. R. Jasperse, Geophys. Res. Lett. **25**, 3485 (1998).
[26]F. S. Mozer and A. Hull, J. Geophys. Res. **106**, 5763 (2001).
[27]P. H. Reiff, H. L. Collin, J. D. Craven, J. L. Burch, J. D. Winningham, E. G. Shelley, L. A. Frank, and M. A. Friedman, J. Geophys. Res. **93**, 7441 (1988).
[28]J. L. Burch, Adv. Space Res. **8**, 353 (1988).
[29]C. Gurgiolo and J. L. Burch, J. Geophys. Res. **93**, 3989 (1988).
[30]J. P. McFadden, C. W. Carlson, and M. H. Boehm, J. Geophys. Res. **95**, 6533 (1990).
[31]R. E. Ergun, C. W. Carlson, J. P. McFadden, F. S. Mozer, and R. J. Strangeway, Geophys. Res. Lett. **27**, 4053 (2000).
[32]F. S. Mozer and C. A. Kletzing, Geophys. Res. Lett. **25**, 1629 (1998).
[33]R. E. Ergun, C. W. Carlson, J. P. McFadden, F. S. Mozer, Y.-J. Su, L. Andersson, D. L. Newman, M. V. Goldman, and R. J. Strangeway, Phys. Rev. Lett. **87**, 045003 (2001).
[34]D. L. Newman, M. V. Goldman, R. E. Ergun, and A. Mangeney, Phys. Rev. Lett. **87**, 255001 (2001).
[35]L. Andersson, R. E. Ergun, D. Newman, J. P. McFadden, C. W. Carlson, and Y.-J. Su, Phys. Plasmas **9**, 3600 (2002).
[36]C. W. Carlson, R. F. Pfaff, and J. G. Watzin, Geophys. Res. Lett. **25**, 2013 (1998).
[37]C. W. Carlson, J. P. McFadden, P. Turin, D. W. Curtis, and A. Magoncelli, Space Sci. Rev. **98**, 33 (2001).
[38]R. E. Ergun, C. W. Carlson, F. S. Mozer, G. T. Delory, M. Temerin, J. P. McFadden, D. Pankow, R. Abiad, P. Harvey, R. Wilkes, H. Primbsch, R. Elphic, R. Strangeway, R. Pfaff, and C. A. Cattell, Space Sci. Rev. **98**, 67 (2001).
[39]R. E. Ergun, L. Andersson, D. S. Main, Y.-J. Su, D. L. Newman, M. V. Goldman, C. W. Carlson, J. P. McFadden, and F. S. Mozer, Phys. Plasmas **9**, 3695 (2002).
[40]M. K. Hudson, W. Lotko, I. Roth, and E. Witt, J. Geophys. Res. **88**, 916 (1983).